A Comparative Analysis of CMUT Receiving Architectures for the Design Optimization of Integrated Transceiver Front-Ends

Marco Sautto, *Student Member*, *IEEE*, Alessandro Stuart Savoia, *Member*, *IEEE*, Fabio Quaglia, Giosuè Caliano, *Senior Member*, *IEEE*, and Andrea Mazzanti, *Senior Member*, *IEEE*

***Abstract*—A formal comparison between fundamental RX amplifier configurations for Capacitive Micromachined Ultrasonic Transducers (CMUT) is proposed in this paper. The impact on both RX and the pulse-echo frequency response and on the output SNR are thoroughly analysed and discussed. It is shown that the resistive-feedback amplifier yields a band-pass RX frequency response, while both open-loop voltage and capacitive-feedback amplifiers exhibit a low-pass frequency response. For a given power dissipation, it is formally proved that a capacitive-feedback amplifier provides a remarkable SNR improvement against the commonly adopted resistive feedback stage, achieved at the expense of a reduced pulse-echo center frequency, making its use convenient in low and mid-frequency ultrasound imaging applications. The advantage mostly comes from a much lower noise contributed by the active devices, especially with low-Q, broadband transducers. The results of the analysis are applied to the design of a CMUT front-end in BCD-SOI technology operating at 10MHz center frequency. It comprises a low-power RX amplifier, a high voltage T/R switch and a 100V TX driver. Extensive electrical characterization, pulse-echo measurements and imaging results are shown. Compared to previously reported CMUT front-ends, this transceiver demonstrates the highest dynamic range and state-of-the-art noise performance with RX amplifier power dissipation of 1 mW.**

***Index Terms*—Ultrasonic transceiver, low-noise amplifier, capacitive sensor, sensor interface, capacitive micromachined ultrasonic transducer (CMUT), high-voltage (HV) driver, T/R switch, ultrasound, BCD-SOI.**

I. Introduction

ULTRASOUND imaging is a well-established medical diagnostic technique. Compared with other imaging modalities, such as for example X-ray, ultrasound is harmless to the patient and less expensive while providing real-time imaging capability with adequate resolution for most applications. Piezoelectric materials have dominated the ultrasound transducers technology for a long time but, thanks to the intense research activity in recent years, capacitive micromachined ultrasonic transducers (CMUT) are emerging as a competitive alternative for next generation imaging systems. They offer wide bandwidth, improving resolution, and a wider operating temperature range [1], [2]. Moreover, the MEMS fabrication process allows for high design flexibility, reproducibility, compact size and low cost. These features, paired with an easier integration with the electronic front-end, make CMUT attractive for new imaging systems such as 3D real-time scanners leveraging dense matrices of transducers [3], [4] and portable ultrasound imagers, an emerging class of devices which is rapidly expanding and is expected to have a broad market potential [5]–[7].

The development of optimized transducers as well as highly integrated front-end electronic interfaces is an active area of research [8]–[11]. Compact size, i.e. high integration, low power and high dynamic range are key design targets to enable a widespread deployment of future CMUT-based imaging systems [12].

The main issue in IC design for ultrasound transducers is the co-existence of high-voltage drivers in the transmit path along with low-voltage and low-noise circuits in the receiver. Device stacking in low-voltage technologies has been investigated to deliver up to 10-20V TX pulses [13], [14]. However CMUTs must be driven at 100 V or more to achieve acoustic pressure comparable with piezoelectric transducers [1], mandating the use of high-voltage technologies [15]–[17]. Moreover, CMUTs show high equivalent source impedance leading to high sensitivity of the output SNR to the loading capacitance [18]. Co-design of the TX and RX circuits and possibly integration on the same die are key to minimize the overall parasitic capacitance and achieve performance competitive with piezoelectric transducers. In this framework, the BCD-SOI technology is particularly attractive, providing high-voltage and high-speed devices simultaneously [19], [20].

We have recently proposed a CMUT front-end comprising a TX driver, T/R switch and RX amplifier [21], [22]. Realized in BCD8-SOI technology from STMicroelectronics, the TX delivers up to 100V pulses, while the RX shows 70dB dynamic range with very low noise at 1mW only power dissipation. This paper extends our prior work by providing additional design insights. A thorough comparison between RX amplifier alternatives, aimed at identifying the best solution to optimize the front-end performance is proposed. In addition, more discussions on the measurement results and imaging experiments are presented.

Minimizing the RX current consumption is fundamental to improve the overall power efficiency because the transducer is used to receive the backscattered echoes for most of the time,

M.Sautto and A.Mazzanti are with the Dipartimento di Ingegneria Industriale e dell'Informazione, Università degli Studi di Pavia, Pavia, Italy (e-mail: marco.sautto01@universitadipavia.it).

A. S. Savoia and G. Caliano are with the Dipartimento di Ingegneria, Università degli Studi Roma Tre, Rome, Italy.

F. Quaglia is with STMicroelectronics, Cornaredo (Milan), Italy.

This work is funded by the European Union through the ENIAC JU project DeNeCoR under grant agreement number 324257

pushing investigation of the optimal RX amplifier. Several alternatives have been proposed so far. The most common approach is a trans-resistance amplifier [9], [10], [18], [23] but capacitive-feedback amplifiers [8], [24], [25] and high input impedance stages [26], [27] (i.e. voltage amplifiers) have been proposed as well. Nevertheless, a rigorous comparison between the three alternatives, aimed at identifying differences and the most convenient approach is missing.

After introducing the micromachined transducer and its equivalent electroacoustic model, Section II of the manuscript compares the most popular RX amplifier configurations with respect to pulse-echo frequency response, noise and power dissipation. It is formally concluded that a charge sensitive amplifier is the most convenient approach for the adopted transducer. Section III presents the main features offered by the BCD-SOI technology and describes in detail circuit design of the front-end building-blocks. Techniques aimed at minimizing silicon area occupation and the loading of the large parasitic capacitances introduced by the high-voltage devices in the TX and T/R switch are discussed. Extensive measurement results and ultrasound imaging experiments are shown in Section IV. Compared to previously reported CMUT front-ends, the proposed realization achieves the best dynamic range and noise-power performance. These features, paired with the ability to drive the transducer with high voltage pulses, enable performance competitive with piezoelectric transducers.

II. CMUT RX Amplifiers Comparison

The CMUT is an electro-acoustic transducer consisting of an array of capacitors, each one realized with a thin flexible plate suspended above a substrate. To transmit acoustic power, the plate can be made to vibrate by applying a time-varying voltage between the two capacitor electrodes. Conversely, when the transducer is used to detect the acoustic pressure, the incident wave causes vibrations of the plate and variation of the equivalent capacitance.

The CMUT RX interface circuit has to detect the capacitance variations generated by the impinging acoustic waves. In view of integration of large arrays, the power budget for each receiver may be very small. At the same time, high SNR and dynamic range are critical not to compromise image quality. Different RX amplifier configurations have been proposed for CMUTs. The amplifier configuration has a significant impact on the overall performance but a comparative discussion among different alternatives has not been reported in literature. The transfer function and input impedance (determining the transducer loading) affect the pulse-echo frequency response. Moreover, for a given power budget, the amplifier configuration has a remarkably different impact on the output SNR.

After introducing the electro-acoustic characteristics of the transducer, this section compares the most popular CMUT RX amplifier configurations. The influence on the pulse-echo frequency response is analysed and the noise performance is compared in order to identify the most convenient solution to achieve best SNR for a given power budget.

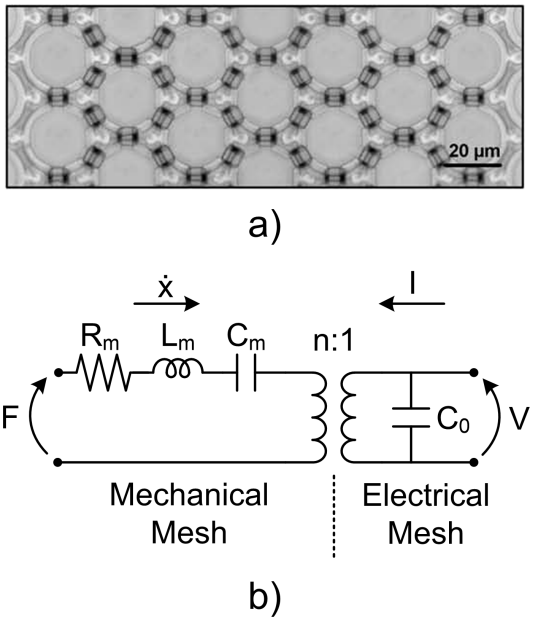

Figure 1: Microphotograph of the CMUT transducer and equivalent electro-mechanical circuit model.

Table I: Components value of the CMUT equivalent circuit model

R_m	500 mΩ
C_m	27.5 nF
L_m	3.5 nH
C_0	9.2 pF
n	0.01

A. CMUT description

The front-end presented in this work is designed for a CMUT array comprising 192 transducers elements, provided with their own individual electrodes, and sharing one common electrode. A microphotograph of a small part of a transducer element, realized with 637 circular cells of 29.6µm diameter in parallel is shown in Fig. 1(a). Width and length of the single element are 200 μm and 3 mm respectively. The detailed geometry of the single CMUT cell, i.e the diameter and thickness of the plate, the gap height, as well as the microfabrication process, packaging technology and probe assembly are described in [1] and [2]. The transducer was designed for pulse-echo operation using receive voltage readout, with a 12MHz center frequency and a -6dB fractional bandwidth greater than 100% when biased at 220 V.

The equivalent circuit in Fig. 1(b) is commonly adopted to model the electro-mechanical operation of the transducer, linearized around a bias point [28]. The circuit is a two-port network composed of two sides coupled by a transformer, which mimics the electro-acoustic energy conversion of the transducer. C_0 and n are proportional to the CMUT area, while C_m, L_m, R_m are inversely proportional [29]. The effect of the electrostatic nonlinearity on the small signal behavior, i.e. the spring-softening effect [30], is lumped in C_m.

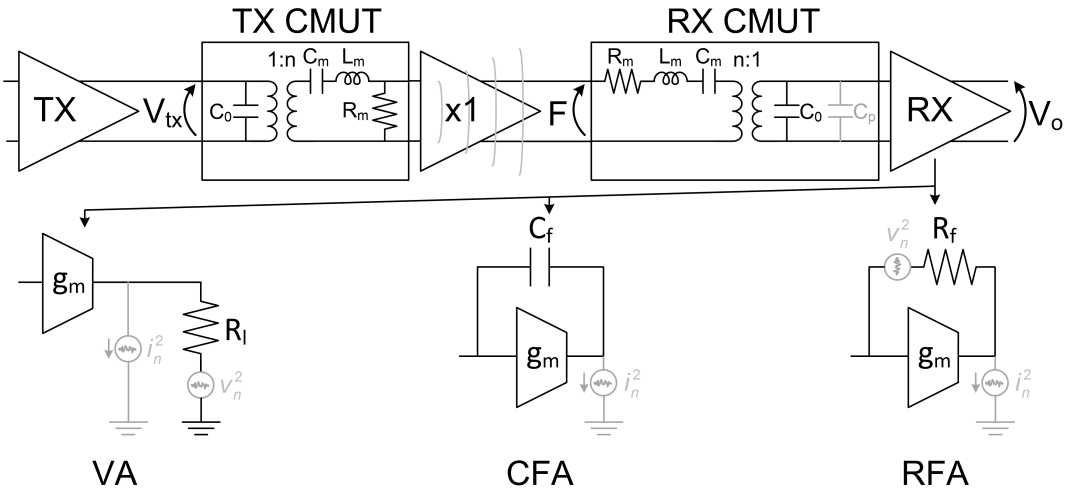

Figure 2: Block diagram adopted to simulate the pulse-echo response with different RX amplifier configurations.

A common figure of merit is the electromechanical conversion factor, normalizing the mechanical energy to the total energy: $k_T^2 = \frac{E_{mech}}{E_{mech}+E_{elec}} = \frac{n^2 C_m}{n^2 C_m + C_0}$ (being E_{mech} and E_{elec} the mechanical and electrical energy respectively) [31].

The transducer shows best performance, i.e. maximum transmit efficiency and receive sensitivity, when the plate is inflected with high DC bias voltage applied between the CMUT electrodes [31]. The component values of the equivalent circuit model, estimated through finite element simulations and measurements of the CMUT biased at 270 V are reported in Table I. The electromechanical conversion factor is 0.23.

B. RX amplifiers and pulse-echo frequency response.

To analyse the impact of the RX amplifier on the pulse-echo frequency response we consider the equivalent circuit depicted in Fig. 2 [29]. Two CMUTs are considered to model the roundtrip path. A transmitter drives the electrical side of the TX CMUT. The TX voltage, V_{tx}, is converted into a force delivered to the RX CMUT[1]. An ideal unity gain buffer separates the two transducers emulating the propagation in a lossless linear medium, provided with a perfect acoustic reflector, without taking into account for diffraction. The RX CMUT converts the incident force, F, to an electrical signal sensed by the RX amplifier. The three alternatives shown in Fig. 2 are evaluated: an open-loop voltage amplifier (VA), a resistive-feedback amplifier (RFA) featuring a trans-resistance gain R_f and a capacitive-feedback amplifier (CFA) with a trans-impedance gain $(\omega C_f)^{-1}$. A broadband transconductor, the simplest low-power active stage in CMOS technology, is assumed as active stage for the three amplifiers. C_p in Fig. 2 represents the parasitic capacitance loading the transducer, due for example to the interconnection between the cells to the amplifier and the input impedance of the transconductor.

[1]When excited by large TX voltage signals, as in typical US imaging driving conditions, the CMUT has a non-linear voltage-to-pressure response. Nonetheless, the adoption of a small-signal model is justified by the fact that the TX voltage-to-pressure response is band-pass and the purpose of the analysis is to compare the pulse-echo frequency response with different RX configurations, for a fixed TX pressure. Moreover, the small-signal modeling approach allows deriving closed form expressions in the analytical comparative analysis here proposed.

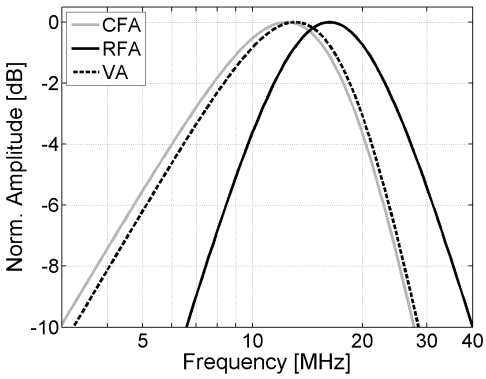

Figure 3: Simulated pulse-echo responses with different RX amplifier configurations.

Fig. 3 compares the normalized pulse-echo responses (i.e. the transfer functions from the driving voltage to the output of the RX amplifiers) assuming the components listed in Table I for the CMUT equivalent circuits and C_p=10 pF. The VA and CFA feature the same shape of the pulse-echo frequency response with only a negligible difference in the center frequency and bandwidth. On the contrary, the RFA displays a remarkably different frequency response. To gain further insights, closed form equations for the transfer functions are derived. By inspection of the circuit in Fig. 2, the incident acoustic force on the RX CMUT is:

$$F = sV_{tx}R_m n C_m H(s, \omega_n, Q) \tag{1}$$

with

$$H(s, \omega_n, Q) = \frac{\omega_n^2}{s^2 + s\frac{\omega_n}{Q} + \omega_n^2} \tag{2}$$

where ω_n and Q are determined only by the mechanical

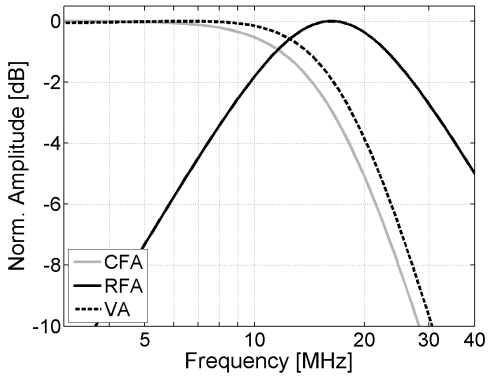

Figure 4: Simulated RX sensitivities.

properties of the CMUT:

$$\omega_n = \frac{1}{\sqrt{C_m L_m}}, \quad Q = \frac{1}{R_m}\sqrt{\frac{L_m}{C_m}} \tag{3}$$

The receive sensitivity, S_{F-V_o}, defined as the gain from F to V_o, i.e. the voltage at the output of the RX amplifiers, depends from the amplifier configuration (the pressure to V_o sensitivity can be calculated by multiplying S_{F-V_o} by the area of the transducer). Assuming sufficiently high transconductance (g_m) of the active stage, the RFA and CFA load the RX CMUT with low impedance[2]. As a result, the electrical capacitors C_0 and C_p are shorted and do not affect the receive sensitivities, given by:

$$S_{F-V_o}|_{RFA} = -sR_f n C_m H(s, \omega_n, Q) \tag{4}$$

$$S_{F-V_o}|_{CFA} = -\frac{1}{C_f} n C_m H(s, \omega_n, Q) \tag{5}$$

The VA displays high input impedance and provides an output voltage proportional to the voltage drop across the C_0 and C_p:

$$S_{F-V_o}|_{VA} = A_v \frac{1}{n} \frac{C_m n^2}{C_m n^2 + (C_0 + C_p)} H(s, \omega_n', Q') \tag{6}$$

where $A_v = g_m R_l$ and $H(s, \omega_n', Q')$ is given by (2) by replacing the following expressions for the natural frequency and quality factor:

$$\omega_n' = \frac{1}{\sqrt{C_{eq} L_m}}, \quad Q' = \frac{1}{R_m}\sqrt{\frac{L_m}{C_{eq}}} \tag{7}$$

$$\text{with } C_{eq} = \frac{C_m (C_0 + C_p)}{C_m n^2 + (C_0 + C_p)}$$

Fig. 4 plots the RX transfer functions, (4)-(6), normalized to the peak gain. The VA and CFA amplifiers display similar low-pass responses. The gain with the VA configuration is impaired by the parallel combination of C_0 and C_p. In fact, at low frequency the latter form a voltage divider with the equivalent mechanical capacitance reported to the electrical side of the transformer, $n^2 C_m$. The larger is $(C_0 + C_p)$, the lower is S_{F-V_o}, confirmed by (6). The natural frequency and quality factor of the VA transfer function, given by (7), are dependent on $(C_0 + C_p)$ through C_{eq}. Nonetheless the impact is mild because $n^2 C_m$ is typically quite smaller than C_0 alone (~3.3 times for the transducer considered in this work) leading to $\omega_n' \sim \omega_n$ and $Q' \sim Q$.

Differently from the CFA and VA, the RFA yields a bandpass transfer function showing a sensitivity peak at the CMUT natural frequency and the same center frequency of the pulse-echo response. The reason can be physically explained as in [23]. The output voltage of the RFA is proportional to the current flowing through the right-side winding of the transformer in the CMUT equivalent circuit, and the latter is proportional to the current in the mechanical branch. If the CMUT is connected to the CFA or VA, its output current is integrated by the feedback capacitor C_f or by the capacitance $(C_0 + C_p)$ respectively. At frequencies close to the CMUT resonance, given by eq. (3), the mechanical impedance of the CMUT is dominated by the mechanical loss and the radiation resistance. Therefore, the L_m-C_m-R_m series in the equivalent circuit of Fig.1 can be approximated with R_m only, and the current, representing the velocity of the membrane, is proportional to the incident force (or pressure). At frequencies lower than the CMUT resonance, the mechanical impedance of the CMUT is dominated by the plate compliance C_m, and the current is proportional to the derivative of the incident force (or pressure).

As a result, if the transducer is operated around the natural frequency ω_n, the RFA provides an output voltage V_o proportional to the incident acoustic force (or pressure). On the other hand, if the transducer is operated below the natural frequency ($\omega < \omega_n$), the CFA and VA provide an output voltage V_o approximately proportional to the incident acoustic force (or pressure), while the output voltage of the RFA is proportional to its derivative, evinced from the zero at the origin in eq. (4).

In any case, the RFA provides a bandpass RX transfer function with a sensitivity peak at the natural frequency and a shape similar to the TX transfer function, while the CFA and VA low-pass frequency shape RX transfer functions are responsible for the low-frequency shift of the corresponding pulse-echo transfer functions in Fig. 3.

Multiplying (1) by (4)-(6), the center frequency of the pulse-echo frequency responses are derived with straightforward calculations:

$$f_0|_{RFA} = \frac{\omega_n}{2\pi}, \quad f_0|_{CFA} \approx f_0|_{VA} = \frac{\omega_n}{2\pi} k_f \tag{8}$$

where $k_f = \sqrt{\left(2Q^2 - 1 + \sqrt{16Q^4 - 4Q^2 + 1}\right)/6Q^2}$ increases with Q until saturation to ~1 for Q > 2. For the CMUT considered in this work Q=0.713, yielding k_f=0.76. The pulse-echo center frequency with the RFA is 16.2 MHz while with the CFA or VA it is 12.3 MHz. Despite different center frequencies, the -6dB bandwidths are comparable. The bandwidth with the RFA is 22.5MHz (8.3MHz-30.8MHz) while with the CFA or VA it is 18MHz (4.6MHz-22.6MHz).

C. Noise Analysis

To compare the noise performance of the three amplifiers, the noise sources are shown in Fig. 2. $i_n^2 = 4kT\gamma g_m$ is

[2]The amplifiers active stage considered in the analysis is a transconductor. At first order, the input impedance of the RFA and CFA is $1/g_m$, and is independent from the value of R_f or C_f.

the noise of the transconductors (being k the Boltzmann's constant, T the absolute temperature and γ a proportionality constant) while $v_n^2 = 4kTR_{l,f}$ is the noise of R_l or R_f in the VA and RFA respectively. To simplify calculations, the transducer equivalent circuit can be approximated as a resistor R_m/n^2 (i.e. the mechanical resistance scaled down by the transformer turn ratio) in parallel with C_0 [18], [32]. The approximation, valid at ω_n, holds over a relatively wide frequency range with broadband transducers because of the low Q. Moreover, since the reactance of $C_0 + C_p$ at ω_n is typically much lower than R_m/n^2 (~0.5 kΩ vs 5 kΩ in our case), for noise calculations the source impedance of the RX amplifiers is further approximated with only C_0 and C_p in parallel. In this condition the input noise PSDs, derived from circuit analysis, are:

$$F_{n,in}^2\big|_{CFA} \approx \frac{1}{n^2 C_m^2 \left|H(s,\omega_n,Q)\right|^2} \frac{4kT\gamma}{g_m} \left(C_0+C_p\right)^2 \quad (9)$$

$$F_{n,in}^2\big|_{VA} \approx \frac{1}{n^2 C_m^2 \left|H(s,\omega_n',Q')\right|^2} \cdot \left(\underbrace{\frac{4kT\gamma}{g_m}\left(C_0+C_p\right)^2}_{\mathrm{g_m noise}} + \underbrace{\frac{4kT}{g_m^2 R_l}\left(C_0+C_p\right)^2}_{\mathrm{R_l noise}} \right) \quad (10)$$

$$F_{n,in}^2\big|_{RFA} \approx \frac{1}{n^2 C_m^2 \left|H(s,\omega_n,Q)\right|^2} \cdot \left(\underbrace{\frac{4kT\gamma}{g_m}\left(C_0+C_p\right)^2}_{\mathrm{g_m noise}} + \underbrace{\frac{kT}{\pi^2 f^2 R_f}}_{\mathrm{R_f noise}} \right) \quad (11)$$

the three conditions $g_m/\left(C_0+C_p\right) \gg \omega_n$, $R_f\left(C_0+C_p\right) \gg 1/\omega_n$, $C_f \ll \left(C_0+C_p\right)$ are assumed to simplify (9) and (11)[3]. The condition $\left(C_0+C_p\right) \gg n^2 C_m$, as previously explained, is assumed to simplify (10). Notably, the contribution of g_m noise is the same for the three amplifiers and the CFA enjoys the lack of additional noisy components. On the other hand, the three amplifiers provide gain over different frequency intervals (see Fig. 3) and a fair noise comparison requires integration of the equivalent input-noise PSD over the bandwidth of the corresponding responses. Unfortunately, this entails calculation of integrals not yielding a simple closed-form expression. To circumvent the issue, noise performance of the three amplifiers are evaluated by comparing the output noise with components sized for the same peak receive sensitivity (gain). The output noise power spectral densities, derived from circuit analysis, are:

$$V_{n,out}^2\big|_{CFA} \approx \frac{4kT\gamma}{g_m}\left(\frac{C_0+C_p}{C_f}\right)^2 \quad (12)$$

$$V_{n,out}^2\big|_{VA} = 4kT\gamma g_m R_l^2 + 4kTR_l \quad (13)$$

$$V_{n,out}^2\big|_{RFA} \approx \frac{16\pi^2 kT\gamma}{g_m} f^2 R_f^2 \left(C_0+C_p\right)^2 + 4kTR_f \quad (14)$$

Eq. (12) and (13) reveal a flat PSD for the CFA and VA while the first term in (14), representing the noise PSD contributed by the transconductor in the RFA, is frequency dependent. For noise comparison, we consider an equivalent PSD, calculated by averaging (14) over $[f_{min} - f_{max}]$, the -3dB bandwidth of the RFA frequency response (-6dB bandwidth of the pulse-echo response):

$$\overline{V_{n,out}^2|_{RFA}} = \frac{\int_{f_{min}}^{f_{max}} V_{n,out}^2\big|_{RFA}}{f_{max}-f_{min}} = \frac{4kT\gamma}{g_m} R_f^2 \left(C_0+C_p\right)^2 \omega_n^2 \left(\frac{3Q^2+1}{3Q^2}\right) + 4kTR_f \quad (15)$$

If, making use of (4)-(6), C_f, R_l and R_f are selected to have the amplifiers with the same receive sensitivity, S_{F-V_o}, at the center frequency of the corresponding pulse-echo response (ω_n for the RFA and $k_f\omega_n$ for the VA and CFA), (12) - (14) can be rewritten:

$$V_{n,out}^2\big|_{CFA} \approx \frac{4kT\gamma}{g_m}\left(\frac{C_0+C_p}{C_m n}\right)^2 \frac{S_{F-V_o}^2}{\left|H(s=jk_f\omega_n)\right|^2} \quad (16)$$

$$V_{n,out}^2\big|_{VA} \approx \underbrace{V_{n,out}^2\big|_{CFA}}_{\mathrm{g_m noise}} + \underbrace{\frac{4kT}{g_m} S_{F-V_o} \frac{C_0+C_p}{C_m n} \frac{1}{QG(Q)}}_{\mathrm{R_l noise}} \quad (17)$$

$$\overline{V_{n,out}^2\big|_{RFA}} \approx \underbrace{V_{n,out}^2\big|_{CFA} D(Q)}_{\mathrm{g_m noise}} + \underbrace{4kT \frac{S_{F-V_o}}{C_m n Q \omega_n}}_{\mathrm{R_f noise}} \quad (18)$$

$$\text{with } G(Q) = \frac{\left|H(s=jk_f\omega_n)\right|}{Q} = \left(\sqrt{Q^2k_f^4 - 2Q^2k_f^2 + Q^2 + k_f^2}\right)^{-1}$$

$$\text{and } D(Q) = G(Q)^2\left(\frac{3Q^2+1}{3Q^2}\right) \approx \left(\frac{1}{(1.50Q-0.23)^2}+1\right).$$

Noise generated by the transducer has not been considered in the analysis. It can be represented by a voltage source in series with R_m in the RX CMUT of Fig. 2 [33]. Since it experiences the same transfer function of the impinging force, if the amplifiers are designed to have the same receive

[3]The conditions are commonly satisfied if the CFA and RFA are designed to achieve sufficient gain and a bandwidth larger than the transducer bandwidth.

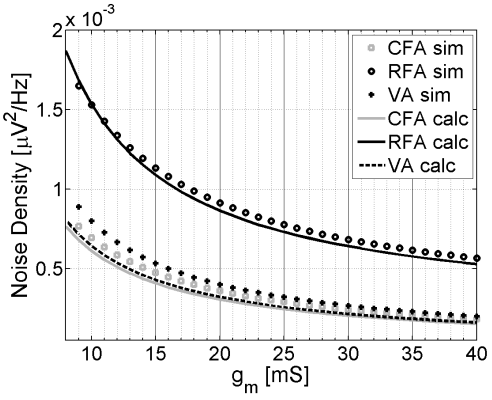

Figure 5: Simulated and calculated RX amplifiers output noise power spectral density.

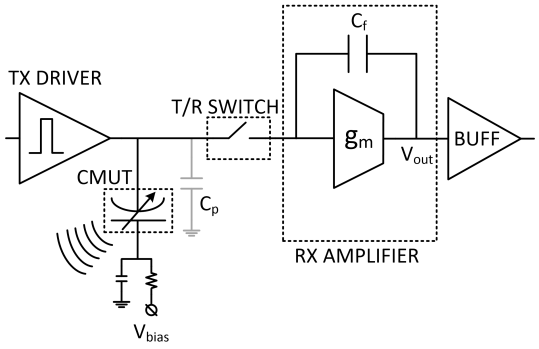

Figure 6: Block diagram of the CMUT transceiver front-end.

sensitivity the contribution to the output noise is the same in the three cases.

Useful insights on the noise performance of the three amplifiers can be derived by looking at eq. (16)-(18). First, notice that even if the three amplifiers have comparable bandwidth, by focusing on PSDs, rather than integrated values, the noise performances are decoupled from the actual bandwidth. From (16)-(18), minimizing C_p, i.e. the parasitic capacitance loading the CMUT, is crucial to limit noise in all the configurations. Moreover, for a given g_m, (16)-(18) demonstrate that the CFA configuration yields the best noise performance. g_m contributes almost to the same noise in the CFA and VA but the latter suffers from small additional noise introduced by the load resistor. The RFA, which is the most widely adopted CMUT amplifier, has the worst noise performance. The relative contribution of the feedback resistor noise in the RFA depends significantly from the design target, i.e. low power or low noise. The transconductance of the active stage sets the power dissipation of the amplifier. Looking at eq.(15), the noise of R_f is independent from g_m, and hence power dissipation, while the contribution of the active stage is inversely proportional to g_m (for all the three configurations). Therefore, in a design targeting low noise, power can be rised to achieve high transconductance gain and R_f becomes the major noise contributor. In this scenario the CFA enjoys better noise performance, not requiring the noisy resistance. In a design targeting low power consumption, g_m becomes the most important noise contribution. In this case, the CFA still enjoys better noise performance due to a remarkably lower g_m noise contribution. As an intuitive explanation, the input noise PSD due to g_m noise is the same for the two amplifiers (see eq. (9), (11)), but it rises with frequency. The CFA has a pulse-echo response centered at lower frequency, where the g_m equivalent input noise PSD is (on average) lower than for the RFA. From (18), g_m noise in the RFA is the same of the CFA multiplied by D(Q). The latter is a monotonic decreasing function of Q ranging from 5.25 for Q=0.5 to ~1 for Q>2. Hence, g_m noise contribution in the RFA is larger than in the CFA and VA, especially for low-Q broadband transducers. With the CMUT adopted in this work, featuring Q=0.713, D(Q)=2.46.

To gain further insights and prove the validity of the analysis, the simulated output noise for the three amplifiers at different g_m is shown in Fig. 5 and compared against (16)-(18). The amplifiers have been designed to achieve a peak sensitivity S_{F-V_o}=200 V/N, requiring $R_f = 12.15\ k\Omega$ and $C_f = 1\ pF$ in the RFA and CFA respectively. The RX transfer functions, normalized to the peak gain, are reported in Fig. 4. The g_m noise proportionality constant is γ=1. Despite the approximations introduced in the analysis, simulations and calculations are in good agreement. At g_m=10 mS the simulated output noise voltage PSD of the RFA is 1.5x10^{-15} V^2/Hz, ~2.2 times larger than with the CFA, mostly due to higher contribution from the transconductor noise (noise of R_f is only 0.2x10^{-15} V^2/Hz, i.e. 13% of the total). The noise PSD of the three amplifiers benefits from a larger transconductance. If g_m is rised to 30 mS, the noise PSD of the RFA is reduced to 0.68x10^{-15} V^2/Hz, but it is 2.83 times larger than with the CFA. As expected, the higher relative contribution of R_f noise (still 0.2x10^{-15} V^2/Hz, i.e. 29% of the total) rises the advantage of the CFA in designs based on higher g_m.The CFA and VA have very similar performance, being the impact of R_l noise in the VA negligible. However, it is worth to remember, by comparing (5) and (6), that the VA gain is sensitive to C_p while the CFA is not. C_p absorbs also the parasitic coupling capacitance between adjacent transducers and the VA is expected to provide low immunity to crosstalk between nearby transducers, responsible for image quality degradation. The CFA is therefore preferable in view of integration of dense CMUT arrays. Moreover, the feedback architecture of the CFA suppresses the distortion introduced by the transconductor leading to higher dynamic range.

It is also worth remembering that the RFA provides a bandpass RX transfer function and, consequently, a pulse-echo frequency response centered at the CMUT natural frequency, yielding increased sensitivity at higher frequencies as compared to VA and CFA. Therefore, as far as high-frequency applications are foreseen, RFA is likely to be preferred.

III. Integrated Front-End Circuits Design

Fig. 6 shows the block diagram of the CMUT transceiver front-end. The design leverages the BCD8-SOI technology from STMicroelectronics, an evolution of the BCD technology with junction isolations replaced by SiO_2 dielectric. It offers three thin and one thick metal layers, high-voltage devices,

and low-voltage, high-speed 0.18µm and 0.35µm CMOS transistors withstanding 1.8V and 3.3V maximum voltage swing respectively. High voltage devices, adopted in the design, are DMOS (either N- and P-channel) with 1µm minimum gate length supporting maximum V_{GS} and V_{DS} of 3.3 V and 100 V respectively. The SOI isolation limits parasitic capacitances improving speed and power dissipation. Moreover, in view of integration of many transceivers on the same chip, the better isolation performance of SOI, compared to PN junctions, enables a much more compact layout and significant area saving.

The transceiver front-end comprises a high-voltage TX driver, a T/R switch and a low-noise RX amplifier, followed by buffer for measurement purposes. The transceiver is connected to the individual electrode of the CMUT array element, while an R-C network is used to apply the bias voltage to the common electrode of the CMUT array. If a positive biasing DC voltage is applied to the common electrode, the resulting voltage across the CMUT during TX is less or equal to the absolute value of the bias voltage, thus preventing the CMUT itself from collapsing. Such approach makes it possible to maximize the CMUT receive sensitivity by applying a bias voltage close to the collapse voltage. Detailed descriptions of the design and optimization of the building blocks are provided in the following subsections.

A. RX amplifier

The RX amplifier in Fig. 6 is realized with a transconductor and the feedback capacitor C_f. From eq. (5), the gain from the impinging force to the output voltage is set solely by transducer parameters and C_f. Given the transducer capacitance and the parasitic capacitance C_p, the transconductance of the active stage, g_m, sets the bandwidth and noise performance and its selection determines the power consumption. The estimated value of C_p is ~10 pF. The relatively large value is because the CMUT is interfaced to the front-end through a PCB connector. By leveraging advanced packaging or 3D integration to place the CMUT in closer proximity to the front-end, C_p is expected to reduce drastically, leading to a substantial performance improvement.

Approximating the source impedance of the amplifier with a capacitor of value $C_0 + C_p$, and assuming negligible capacitance loading the amplifier output node, the -3dB amplifier bandwidth is given by:

$$BW \approx \frac{g_m}{C_0 + C_p} \tag{19}$$

As a rule of thumb, a minimum constrain for the g_m can be found imposing the amplifier bandwidth to be at least twice the resonance frequency of the transducer, $g_m > 2\omega_n (C_0 + C_p)$ = 3.9 mS.

According to eq. (16) in Section II and the plot shown in Fig. 5, the higher g_m and the lower is the amplifier noise. We target a noise contribution from the amplifier comparable to the noise of the transducer and the estimated g_m is 10 mS, larger than what required to satisfy the -3dB bandwidth constraint. The feedback capacitance is set to 1 pF, providing a receive sensitivity of 232 V/N.

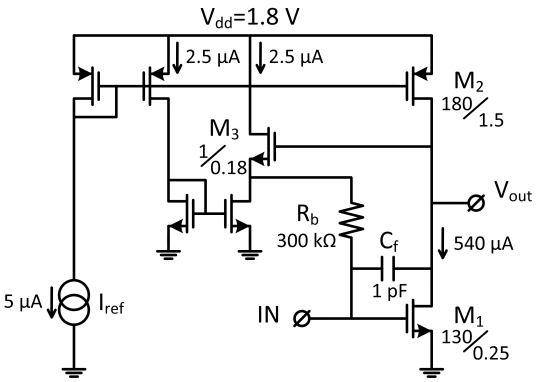

Figure 7: Schematic of the RX amplifier.

The schematic of the amplifier is shown in Fig. 7. Power dissipation is set to 1 mW, corresponding to 550 μA from the 1.8 V supply. Transistor M_1, sized for g_m=10 mS, determines the transconductance of the stage. M_2 sets the bias current to M_1, by mirroring I_{ref}. The level shifter M_3 and resistor R_b are used for biasing the gate of M_1. Compared to a simple resistor, the use of a level shifter sets the output quiescent voltage to $V_{gs1} + V_{gs3}$ (≈550 mV+400 mV), close to V_{dd}/2, maximizing 1dB compression point and hence the amplifier dynamic range. The level shifter is biased at low current density by the nMOS current mirror. R_b introduces a zero at DC and a pole at frequency $1/(2\pi C_f R_b)$ in the transfer function and a large value has been selected to push the pole at sufficiently low frequency (≈530 kHz). The size of M_1 has been selected to achieve the desired transconductance with a non-minimum channel length to limit the in-band 1/f noise contribution.

B. TX Driver

The high-voltage TX driver is shown in Fig. 8(a). Transistors M_4-M_5 provide unipolar pulses of 100 V across the CMUT electrodes during transmission. Device aspect ratios are 1600µm/1µm and 4100µm/1µm. Large size is selected to achieve rise and fall time of ≈ 15 ns, suited for an excitation frequency of 10 MHz. The reverse biased drain-to-bulk junctions, represented by the diodes in the DMOS symbols, load node-A with a large parasitic capacitance, $C_{j4} + C_{j5}$ ≈ 5 pF. Diodes D_1-D_2 are used to disconnect the CMUT from node-A during reception, when M_4 and M_5 are off. In this case the CMUT is loaded approximately by the parasitic capacitance of D_1 - D_2 of 90 fF only, much lower than $C_{j4} + C_{j5}$, thus preventing a significant SNR penalty.

The TX driver is controlled by 1.8V input pulse trains. To prevent simultaneous conduction of the output stage devices (M_4-M_5), complementary signals are first provided with a conventional non-overlapping clock generation circuit, implemented with thin-oxide 0.18µm gates. High-voltage transistors occupy large area and, in order to minimize their size (set by the required on-state resistance) they must be driven with the maximum allowed overdrive voltage. Therefore, the 0-1.8V pulse trains at the output of the non-overlapping clock generator are translated to 0-to-3.3V control signals (S_p,

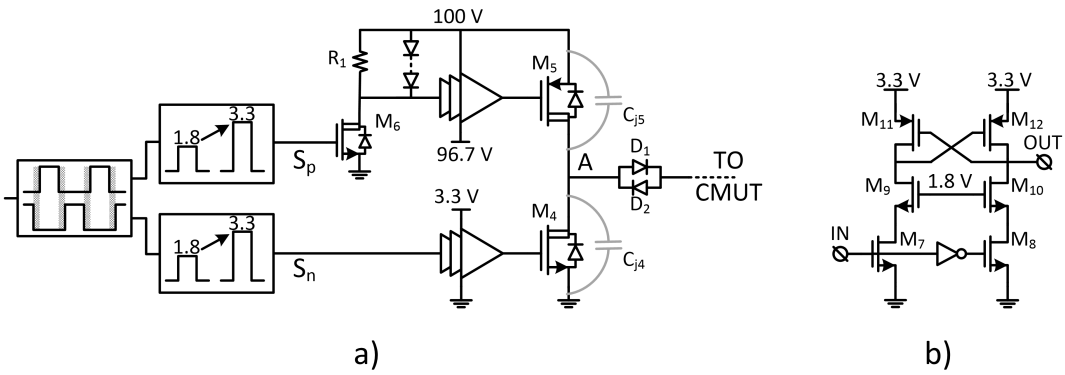

Figure 8: Schematic of the TX driver (a) and low-voltage level shifter (b).

S_n) with the latch-based level shifter shown in Fig. 8(b). It consists of a cross-coupled pair (M_{11}-M_{12}) driven by the input transistors (M_7-M_8), allowing fast commutation with zero static power dissipation. M_9-M_{12} are 0.35µm transistors, able to sustain the 3.3V output swing while M_7-M_8 are thin-oxide devices protected from the large output voltage by M_9-M_{10}.

S_p has to be further translated to a voltage ranging from 96.7 V to 100 V. Different techniques have been reported in literature to realize high voltage shifters. A latch-based architecture, similar to the topology in Fig. 8(b) is proposed in [15]. The drawback is the need for six high-voltage transistors, occupying large area. A more compact solution is adopted in [34] where the level shifter is realized with a simple common-source stage loaded with a diode-connected device. The main issue of this approach is the slowness in the turn-off transition, due to the limited discharging current capability of a diode-connected transistor. Moreover, the active load requires large overdrive to achieve high-voltage swing, mandating selection of high current (and hence power dissipation) or small transistor size, penalizing speed.

In this design, the high-voltage level shifter is realized by M_6 and R_1 in Fig. 8(a). The approach is similar to [34] but the diode-connected load is replaced by R_1, mitigating the above issues and requiring less silicon. The maximum voltage drop on R_1 is limited to 3.3 V by a battery of diodes, ensuring robustness against components spread due to process variations. The high-voltage shifter draws current when M_6 is on. To limit power dissipation, the gate of the high-voltage pMOS M_5 is driven by a tapered buffer chain, scaling the load capacitance of the high-voltage MOS down to 18 fF from 6 pF. An identical buffer chain drives M_4 to match the delays experienced by S_p and S_n. Size of M_6 is 6µm/1µm and R_1=6.4 kΩ. The simulated contribution to power dissipation of the level shifters and driving circuits is less than 10% of the high-voltage output stage.

C. T/R Switch

The schematic of the T/R switch is shown in Fig. 9. DMOS M_{13} withstands the high-voltage TX pulses. It must provide high off-state isolation to protect the sensitive RX amplifier and at the same time low on-resistance to limit SNR

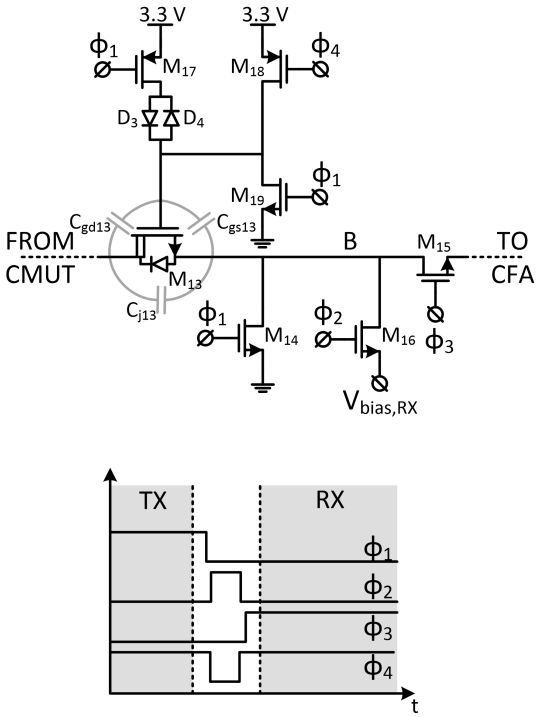

Figure 9: Schematic of the T/R switch (top) and timing of the control signals (bottom).

and bandwidth degradation. To gain insight, considering its channel resistor r_{on} in series to the CFA input, the following expressions for bandwidth and output noise can be derived:

$$BW \approx \frac{1}{(C_0 + C_p)\left(r_{on} + \frac{1}{g_m}\right)} \tag{20}$$

$$N_{out}^2 \approx 4kT\left(r_{on} + \frac{\gamma}{g_m}\right)\left(\frac{C_0 + C_p}{C_f}\right)^2 \tag{21}$$

Thus, not to compromise too much the amplifier performance, r_{on} must be comparable or lower than $1/g_m$. On the other hand, low r_{on} trades with transistor size, leading to large device parasitic capacitances and area occupation. We selected $W_{M_{13}} \approx 100$ µm, leading to $r_{on} \approx 100\ \Omega$ and $C_{par} \approx 1$ pF. Diodes D_3 – D_4, connected to the 3.3 V supply by M_{17}, are

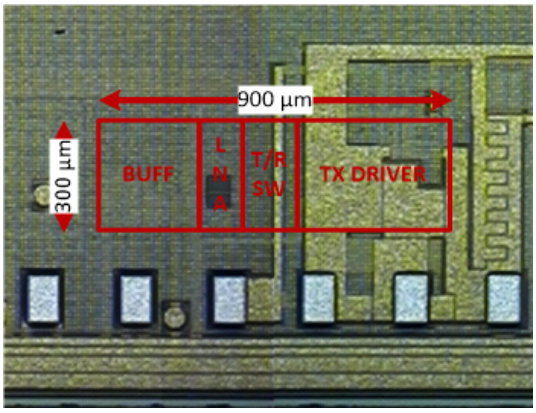

Figure 10: Chip photograph.

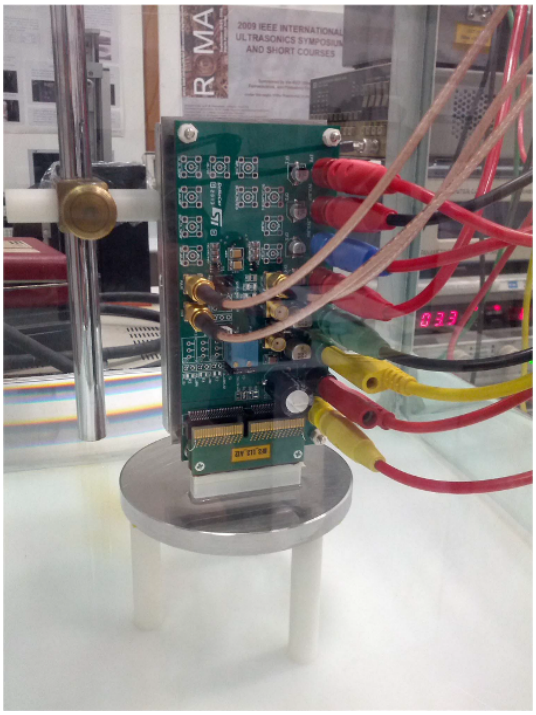

Figure 11: Test board with the CMUT probe head immersed in a water tank.

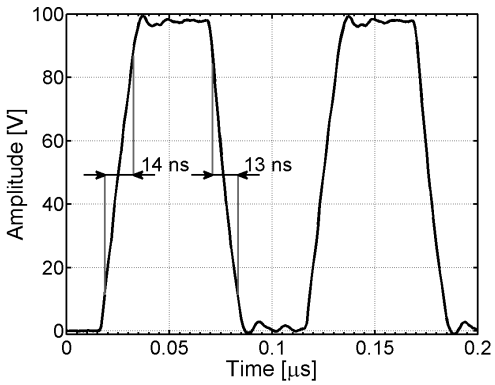

Figure 12: Measured TX pulses at 100V supply.

introduced to decrease the equivalent parasitic capacitance in RX mode to approximately 120 fF. M_{19} keeps the gate of M_{13} well-biased to ground in off-state while M_{18} avoids the diodes voltage drop by bootstrapping the gate control signal when M_{13} is switched on.

A further drawback of choosing a too large width for M_{13} is the penalty in the off-state isolation due to signal leakage through the large parasitic junction capacitance of the drain to bulk diode, C_{j13} in Fig. 9. Most of the previously reported T/R switches [10], [14], [15], [18] are realized with a single high-voltage device in series to the RX amplifier input. The off-state isolation, i.e. the voltage attenuation from the input to the output of the T/R switch, is only 20 dB in our case. Being 100 V the maximum pulser output voltage, the attenuation provided by a single device is not enough to ensure protection of the RX amplifier. To solve this issue transistor M_{14} shunts node-B to ground when M_{13} is off while M_{15}, driven by Φ_3, disconnects the input of the RX amplifier in order to not perturb the DC biasing point. Finally M_{16}, driven by Φ_2, is introduced to speed-up the time required to switch from TX to RX mode by pre-charging the top plate of the CMUT to $V_{bias,RX} = V_{GS,M_1}$ (being V_{GS,M_1} the gate-to-source voltage of M_1 in Fig. 7). With this solution, the simulated settling time to switch between transmission to reception is reduced to 4 µs. Without M_{16} the top plate of the CMUT would have to be charged by the RX amplifier with an excessively long time constant. $V_{bias,RX}$ is a low impedance biasing voltage, generated with a replica of the core transistors in the RX transconductor, that can be shared among several transducers. M_{14}, M_{15}, M_{16} are low-voltage, high-speed transistors introducing negligible parasitic capacitances due to the small dimensions.

IV. Experimental Results

A microphotograph of the realized integrated circuit is shown in Fig. 10. The active die area, excluding the output buffer introduced for measurement purposes, is approximately 0.18 mm^2. Prototypes of the transceiver are bonded directly on a custom designed PCB, which mounts also the connector for the CMUT probe head. Fig. 11 shows a photograph of the test board with the transducer immersed in a water tank. The high voltage required to bias the common electrode of CMUT array (see the block diagram in Fig. 6) is generated with discrete components.

Measured pulses at 10MHz frequency, delivered by the TX driver with 100V supply are shown in Fig. 12. The rise and fall time from 10% to 90% of the peak-to-peak voltage are 14 ns and 13 ns respectively.

Fig. 13 compares the measured and simulated voltage gain of the RX path. In this case, a 10pF capacitor in series with a voltage source replaces the transducer. Measurements and simulations are in good agreement. The peak gain is 14.2 dB, with -3dB bandwidth extending from 500 kHz to 40 MHz. The output voltage at 1dB gain compression, determined through large signal measurements with a sinusoidal excitation, is of 564 mV$_{0-pk}$.

The measured and simulated output noise spectral density is shown in Fig. 14. The 1/f noise corner is ~4MHz. The Noise Figure, calculated by normalizing the total noise to the

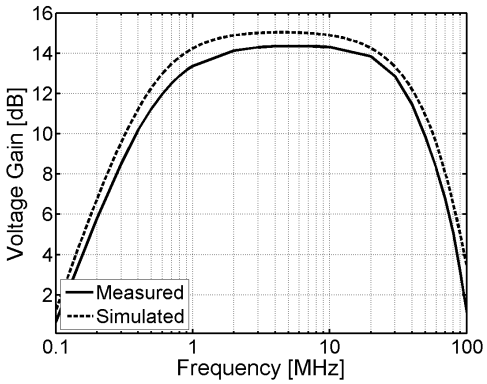

Figure 13: Measured and simulated RX voltage gain.

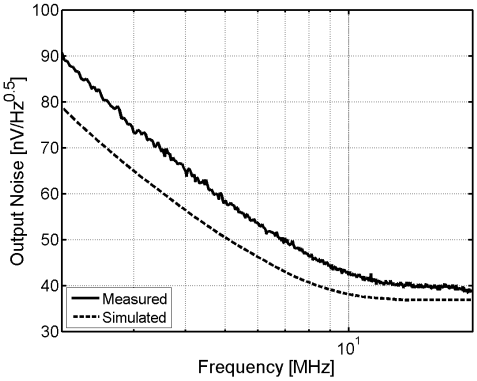

Figure 14: Measured and simulated RX output noise.

estimated contribution of the transducer, is 8.9 dB.

An extensive electro-acoustic characterization has been carried out. For pulse-echo measurements, the probe head was immersed in a water tank, facing a stainless steel planar reflector placed at the elevation focal distance of 1.5 cm. The TX drives the CMUT with pulse trains and the reflected echoes are recorded after switching to RX mode. Fig. 15(a) shows the received signals with a CMUT bias voltage ranging from 150 V to 270 V. The normalized pulse-echo frequency responses, corresponding to the FFT of the received time-domain signals when the transmitter delivers very short isolated pulses of ~20 ns (in order to excite the entire CMUT frequency band) are reported in Fig. 15(b). As expected, bandwidth and center frequency are slightly affected by the CMUT bias voltage due to the spring softening effect [30]. At the maximum value of 270 V, center frequency is 10 MHz and the -6dB bandwidth is ~100%, extending from 4.4 MHz to 15.4 MHz.

The receive sensitivity has been estimated by processing two different measurement sets. The plot in Fig. 16(a) shows the transmitted pressure frequency response, measured with a needle type MHA9-150 hydrophone (Force Technology, Brøndby, Denmark) placed at twice the elevation focal distance of the probe. In this circumstance, it can be assumed that the incident pressure on the hydrophone is the same received by CMUT during the pulse-echo measurements. The receive sensitivity frequency response is then computed by dividing the spectra of the pulse-echo by the transmit sensitivity. The

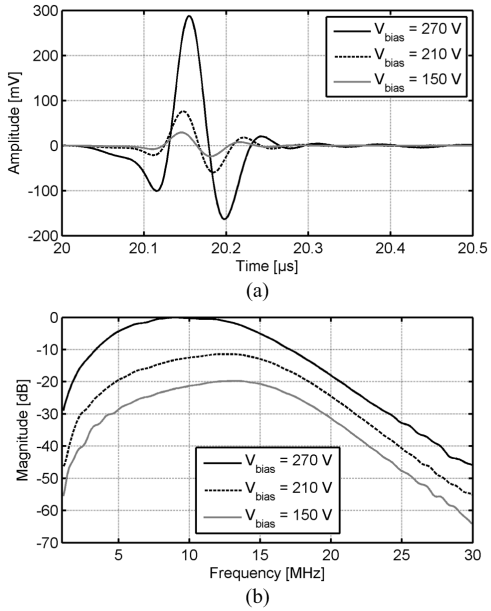

Figure 15: Received echoes (a) and pulse-echo frequency response (b) for different values of the bias voltage, from 150 V to 270 V.

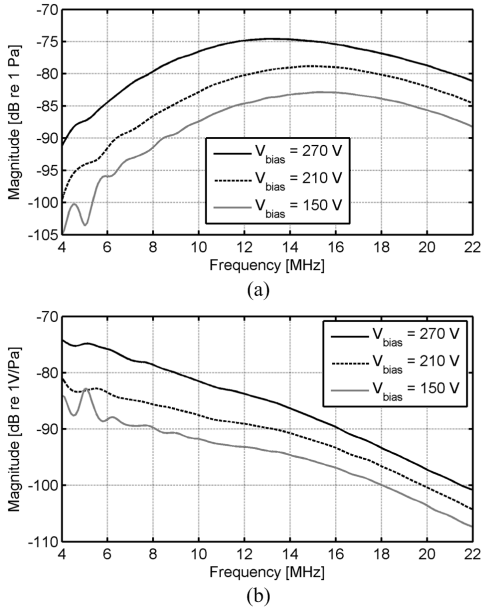

Figure 16: Transmit pressure(a) and receive sensitivity (b) for different values of the bias voltage, from 150 V to 270 V.

resulting curves, reported in Fig. 16(b) display a low-pass shape, as expected from the use of a capacitive-feedback amplifier. However, a quantitative discrepancy between the slope of the experimentally estimated and the simulated frequency responses is observable. This discrepancy is likely due to the fact that the equivalent circuit model used in this paper does not take into account the frequency-dependant acoustic attenuation of the silicone rubber constituting acoustic lens of the CMUT probe. Moreover, the equivalent circuit models the radiation impedance as purely resistive, while the experiments were performed using a limited sized transducer

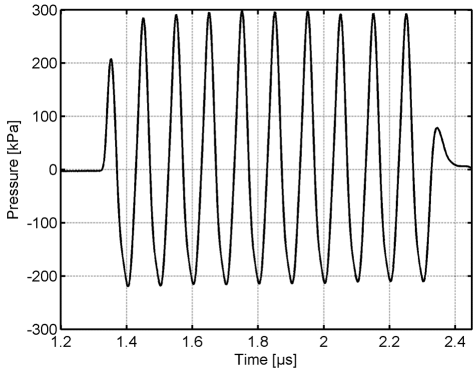

Figure 17: Acoustic pressure measured at 2 mm from the CMUT biased at 270 V and excited with a 100V, 10-cycle burst at 10 MHz.

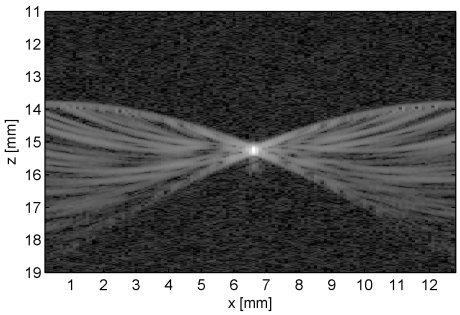

Figure 18: SAF image of a copper wire immersed in water obtained by mechanically scanning the CMUT with a 100µm step. Each scan line is obtained by beamforming 128 signals. The dynamic range of the image is 80 dB.

array element, characterized by a lateral dimension of the order of a wavelength, whose radiation impedance is characterized by a not negligible reactive part, mainly inductive, representing the mass loading of the propagation medium.

With 270V CMUT bias voltage, the receive sensitivity at the center frequency of the pulse-echo response, 10 MHz, is 72 mV/kPa.

The output noise, integrated over the pulse-echo bandwidth, is 133 μV_{rms}, corresponding to an equivalent noise spectral density superimposed to the incident pressure of N_{in} = 0.55 mPa/$\sqrt{\mathrm{Hz}}$. The estimated input pressure at 1dB gain compression is 7.83 kPa and the dynamic range of the receiver, defined by the ratio of the maximum signal at 1dB compression to the minimum signal at SNR=0 dB, is 70 dB.

Furthermore, the transmit pressure generated with the maximum TX pulse amplitude was measured by placing the hydrophone at 2 mm from the transducer surface. The CMUT biased at 270 V was driven with a 100V, 10-cycle burst at 10 MHz. The peak-to-peak amplitude of the pressure signal recorded, shown in Fig. 17, is approximately 500 kPa. The difference in the positive and negative peak amplitudes observable is due to the CMUT nonlinear large-signal response.

Measured electro-acoustic results demonstrate performance comparable to a commercial probe based on piezoelectric transducers operating in the same frequency range [1].

Finally, an ultrasound image of a 40µm-diameter copper wire immersed in water was obtained by mechanically scanning the CMUT and by acquiring the pulse-echo signal at each position. The CMUT was driven in the same conditions of the TX pressure measurements, using a 2-cycle burst at 10 MHz. The 256 rf signals resulting from a 25.6cm scan using a 100µm step were filtered, using a tapered cosine window with -3dB cut-off frequencies of 4.4 MHz and 15.6 MHz, and beamformed with a single-element Synthetic Aperture Focusing (SAF) algorithm using 128-element apertures to form each scan line. The obtained image, normalized to the maximum signal amplitude and log-compressed, is represented in Fig. 18 using a very high dynamic range of 80 dB, in order to make visible both point spread function sidelobes and background noise. The SNR was computed, using the uncompressed rf beamformed data, as the ratio between the rms amplitude of the point target signal S_{rms} and of the noise N_{rms} estimated in a dark portion of the image, resulting in a value of $SNR_m = 20log_{10}\left(\frac{S_{rms}}{N_{rms}}\right) = 66.7$ dB. In order to assess the measured SNR performance, the expected SNR for a 128-element SAF aperture, assuming uncorrelated additive noise for the receiver and neglecting the signal loss due to the array element directivity, was computed from the receiver dynamic range (70 dB), compensated for the ratio between the maximum output voltage of the receiver (564 mV) and the maximum signal amplitude of the acquired rf data (167 mV), resulting in the value of $SNR_e = 10log_{10}(128) + 70 - 20log_{10}\left(\frac{V_{max-o}}{V_{max-rf}}\right) = 80.5$ dB. The 14dB discrepancy between the measured and predicted SNR is partially attributed to the simplifying analytical assumption that the peak signal amplitude is constant for all the scan lines (while acquisitions with the transducer far from the center experience up to 8dB loss) and correlated noise on the supply voltages, not sufficiently filtered out in the experimental setup. Nevertheless, the high excitation voltage of the TX driver, paired with the low noise and high linearity of the RX amplifier, enable excellent image SNR and dynamic range.

The performance of the front-end are summarized and compared against previously reported CMUT front-ends in Table-II. Sufficient information to estimate the transducer electromechanical conversion factor are provided only in [9], yielding k_T^2=0.25, similar to our case. Compared to previous works, the proposed transceiver shows the highest TX pulse amplitude and RX dynamic range. The equivalent input noise is the lowest, similar to [18] but with more than 10x power saving. This has been achieved by identifying the optimal amplifier configuration and through careful circuit design to minimize the amplifier noise generation.

V. Conclusions

A comparison between the fundamental amplifier configurations for CMUT amplifiers has been proposed. Equivalent circuit-based modeling was used to derive closed-form expressions, allowing a clear assessment of the impact of different amplifier configurations on the pulse-echo frequency response

Table II: MEASUREMENT SUMMARY AND COMPARISON

	This Work	[18]	[23]	[9]	[10]	[14]	[8]
CMUT capacitance [pF]	9.2	40	0.15	0.3	1.57	0.23	0.09
k_T^2	0.23	-	-	0.25	-	-	-
Center Frequency [MHz]	10	3	15	2.2	5.1	2.6	20
Bandwidth [MHz]	11	5.2	10	5	6.4	2.6	8.6
Pulse Amplitude [V]	100	30	-	25	25	15	25
RX Sensitivity [$^{\mathrm{mV}}/_{\mathrm{kPa}}$]	72	162	130	414	70	-	-
Input Noise [$^{\mathrm{mPa}}/_{\sqrt{\mathrm{Hz}}}$]	0.55	0.56	3	0.9	1.8	-	-
Noise Figure [dB]	8.9	10.3	1.8	-	-	-	-
Dynamic Range [dB]	70	60	42	-	-	-	50
RX Amp. Power [mW]	1	14.3	6.6	2.4	4	0.328	0.8

and SNR. The study allowed to formally conclude that a capacitive-feedback stage provides a remarkable improvement in the noise-power performance compared to the very popular resistive-feedback amplifier, at the expense of a low-frequency shift of the pulse-echo response, making it suitable for integration of dense CMUT arrays for low and mid-frequency ultrasound imaging applications. Moreover, a CMUT transceiver front-end suitable for mobile ultrasound imaging applications in BCD-SOI technology was presented. By leveraging the results of the analysis and through a careful co-design of the RX and TX circuits aware of the large parasitic capacitances introduced by the high voltage transistors, the transceiver is able to deliver up to 100V pulses while featuring an ultra-low power RX amplifier with a record dynamic range. System functionality has been extensively demonstrated with electrical and pulse-echo measurements.

The comparative analysis presented in this paper was used to select the best architecture for a given CMUT design. However, the methods here proposed can be applied in the context of a CMUT-based imager design, which may include the optimization of both the transducer and the RX amplifier for a given imaging application characterized by its specific TX and RX signal amplitude and frequency requirements, as well as transducer geometry and system power constraints.

REFERENCES

[1] A. Savoia, G. Caliano, and M. Pappalardo, "A CMUT probe for medical ultrasonography: from microfabrication to system integration," *IEEE Transactions on Ultrasonics, Ferroelectrics and Frequency Control*, vol. 59, no. 6, pp. 1127–1138, Jun. 2012.

[2] A. Savoia, G. Caliano, B. Mauti, and M. Pappalardo, "Performance optimization of a high frequency CMUT probe for medical imaging," in *Ultrasonics Symposium (IUS), 2011 IEEE International*, Oct. 2011, pp. 600–603.

[3] L. F. Goncalves, J. Espinoza, J. P. Kusanovic, W. Lee, J. K. Nien, J. Santolaya-Forgas, G. Mari, M. C. Treadwell, and R. Romero, "Applications of 2-dimensional matrix array for 3- and 4-dimensional examination of the fetus: a pictorial essay," *Journal of Ultrasound in Medicine: Official Journal of the American Institute of Ultrasound in Medicine*, vol. 25, no. 6, pp. 745–755, Jun. 2006.

[4] L. F. Goncalves, W. Lee, J. Espinoza, and R. Romero, "Three- and 4-dimensional ultrasound in obstetric practice: does it help?" *Journal of Ultrasound in Medicine: Official Journal of the American Institute of Ultrasound in Medicine*, vol. 24, no. 12, pp. 1599–1624, Dec. 2005.

[5] G.-d. Kim, C. Yoon, S.-B. Kye, Y. Lee, J. Kang, Y. Yoo, and T.-K. Song, "A single FPGA-based portable ultrasound imaging system for point-of-care applications," *IEEE Transactions on Ultrasonics, Ferroelectrics, and Frequency Control*, vol. 59, no. 7, pp. 1386–1394, Jul. 2012.

[6] J. Baran and J. Webster, "Design of low-cost portable ultrasound systems: Review," in *Annual International Conference of the IEEE Engineering in Medicine and Biology Society, 2009. EMBC 2009*, Sep. 2009, pp. 792–795.

[7] K. C. Kim, M. J. Kim, H. S. Joo, W. Lee, C. Yoon, T.-K. Song, and Y. Yoo, "Smartphone-based portable ultrasound imaging system: A primary result," in *Ultrasonics Symposium (IUS), 2013 IEEE International*, Jul. 2013, pp. 2061–2063.

[8] G. Gurun, C. Tekes, J. Zahorian, T. Xu, S. Satir, M. Karaman, J. Hasler, and F. Degertekin, "Single-chip CMUT-on-CMOS front-end system for real-time volumetric IVUS and ICE imaging," *IEEE Transactions on Ultrasonics, Ferroelectrics, and Frequency Control*, vol. 61, no. 2, pp. 239–250, Feb. 2014.

[9] I. Wygant, N. Jamal, H. Lee, A. Nikoozadeh, O. Oralkan, M. Karaman, and B. Khuri-yakub, "An integrated circuit with transmit beamforming flip-chip bonded to a 2-D CMUT array for 3-D ultrasound imaging," *IEEE Transactions on Ultrasonics, Ferroelectrics and Frequency Control*, vol. 56, no. 10, pp. 2145–2156, Oct. 2009.

[10] I. O. Wygant, X. Zhuang, D. T. Yeh, O. Oralkan, A. Sanli Ergun, M. Karaman, and B. T. Khuri-Yakub, "Integration of 2d CMUT arrays with front-end electronics for volumetric ultrasound imaging," *IEEE transactions on ultrasonics, ferroelectrics, and frequency control*, vol. 55, no. 2, pp. 327–342, Feb. 2008.

[11] A. Bhuyan, J. W. Choe, B. C. Lee, I. Wygant, A. Nikoozadeh, O. Oralkan, and B. Khuri-Yakub, "Integrated Circuits for Volumetric Ultrasound Imaging With 2-D CMUT Arrays," *IEEE Transactions on Biomedical Circuits and Systems*, vol. 7, no. 6, pp. 796–804, Dec. 2013.

[12] X. Xu, H. Venkataraman, S. Oswal, E. Bartolome, and K. Vasanth, "Challenges and considerations of analog front-ends design for portable ultrasound systems," in *2010 IEEE Ultrasonics Symposium (IUS)*, Oct. 2010, pp. 310–313.

[13] H.-K. Cha, D. Zhao, J. H. Cheong, B. Guo, H. Yu, and M. Je, "A CMOS High-Voltage Transmitter IC for Ultrasound Medical Imaging Applications," *IEEE Transactions on Circuits and Systems II: Express Briefs*, vol. 60, no. 6, pp. 316–320, Jun. 2013.

[14] A. Banuaji and H.-K. Cha, "A 15-V Bidirectional Ultrasound Interface Analog Front-End IC for Medical Imaging Using Standard CMOS Technology," *IEEE Transactions on Circuits and Systems II: Express Briefs*, vol. 61, no. 8, pp. 604–608, Aug. 2014.

[15] R. Chebli and M. Sawan, "Fully Integrated High-Voltage Front-End Interface for Ultrasonic Sensing Applications," *IEEE Transactions on Circuits and Systems I: Regular Papers*, vol. 54, no. 1, pp. 179–190, Jan. 2007.

[16] D. Bianchi, F. Quaglia, A. Mazzanti, and F. Svelto, "A 90vpp 720mhz GBW linear power amplifier for ultrasound imaging transmitters in BCD6-SOI," in *Solid-State Circuits Conference Digest of Technical Papers (ISSCC), 2012 IEEE International*, Feb. 2012, pp. 370–372.

[17] A. S. Savoia, G. Scaglione, G. Caliano, A. Mazzanti, M. Sautto, and F. Quaglia, "Second-harmonic reduction in CMUTs using unipolar

pulsers," in *Ultrasonics Symposium (IUS), 2015 IEEE International*, Oct. 2015, pp. 1–4.

[18] K. Chen, H.-S. Lee, A. Chandrakasan, and C. Sodini, "Ultrasonic Imaging Transceiver Design for CMUT: A Three-Level 30-Vpp Pulse-Shaping Pulser With Improved Efficiency and a Noise-Optimized Receiver," *IEEE Journal of Solid-State Circuits*, vol. 48, no. 11, pp. 2734–2745, Nov. 2013.

[19] M. Sambi, D. Merlini, P. Galbiati, E. Bonera, and F. Belletti, "A novel 0.16 um - 300 V SOIBCD for ultrasound medical applications," in *2011 IEEE 23rd International Symposium on Power Semiconductor Devices and ICs (ISPSD)*, May 2011, pp. 36–39.

[20] D. Bianchi, F. Quaglia, A. Mazzanti, and F. Svelto, "Analysis and Design of a High Voltage Integrated Class-B Amplifier for Ultra-Sound Transducers," *IEEE Transactions on Circuits and Systems I: Regular Papers*, vol. Early Access Online, 2014.

[21] M. Sautto, D. Leone, A. Savoia, D. Ghisu, F. Quaglia, G. Caliano, and A. Mazzanti, "A CMUT transceiver front-end with 100-V TX driver and 1-mW low-noise capacitive feedback RX amplifier in BCD-SOI technology," in *European Solid State Circuits Conference (ESSCIRC), ESSCIRC 2014 - 40th*, Sep. 2014, pp. 407–410.

[22] A. Savoia, G. Caliano, A. Mazzanti, M. Sautto, A. Leone, D. Ghisu, and F. Quaglia, "An ultra-low-power fully integrated ultrasound imaging CMUT transceiver featuring a high-voltage unipolar pulser and a low-noise charge amplifier," in *Ultrasonics Symposium (IUS), 2014 IEEE International*, Sep. 2014, pp. 2568–2571.

[23] G. Gurun, P. Hasler, and F. Degertekin, "Front-end receiver electronics for high-frequency monolithic CMUT-on-CMOS imaging arrays," *IEEE Transactions on Ultrasonics, Ferroelectrics and Frequency Control*, vol. 58, no. 8, pp. 1658–1668, Aug. 2011.

[24] S.-Y. Peng, M. Qureshi, P. Hasler, A. Basu, and F. Degertekin, "A Charge-Based Low-Power High-SNR Capacitive Sensing Interface Circuit," *IEEE Transactions on Circuits and Systems I: Regular Papers*, vol. 55, no. 7, pp. 1863 –1872, Aug. 2008.

[25] S.-Y. Peng, M. Qureshi, A. Basu, R. Guldiken, F. Degertekin, and P. Hasler, "PS-15 Floating-Gate Based CMUT Sensing Circuit Using Capacitive Feedback Charge Amplifier," in *IEEE Ultrasonics Symposium, 2006*, Oct. 2006, pp. 2425 –2428.

[26] I. Cicek, A. Bozkurt, and M. Karaman, "Design of a front-end integrated circuit for 3d acoustic imaging using 2d CMUT arrays," *IEEE Transactions on Ultrasonics, Ferroelectrics and Frequency Control*, vol. 52, no. 12, pp. 2235 –2241, Dec. 2005.

[27] T. Singh, T. Saether, and T. Ytterdal, "Feedback Biasing in Nanoscale CMOS Technologies," *IEEE Transactions on Circuits and Systems II: Express Briefs*, vol. 56, no. 5, pp. 349–353, May 2009.

[28] W. P. Mason, *Electromechanical transducers and wave filters*. D. Van Nostrand Co., 1948.

[29] G. Matrone, A. Savoia, M. Terenzi, G. Caliano, F. Quaglia, and G. Magenes, "A volumetric CMUT-based ultrasound imaging system simulator with integrated reception and u-beamforming electronics models," *IEEE Transactions on Ultrasonics, Ferroelectrics, and Frequency Control*, vol. 61, no. 5, pp. 792–804, May 2014.

[30] I. Ladabaum, X. Jin, H. Soh, A. Atalar, and B. Khuri-Yakub, "Surface micromachined capacitive ultrasonic transducers," *IEEE Transactions on Ultrasonics, Ferroelectrics, and Frequency Control*, vol. 45, no. 3, pp. 678–690, May 1998.

[31] G. Yaralioglu, A. Ergun, B. Bayram, E. Haeggstrom, and B. T. Khuri-Yakub, "Calculation and measurement of electromechanical coupling coefficient of capacitive micromachined ultrasonic transducers," *IEEE Transactions on Ultrasonics, Ferroelectrics, and Frequency Control*, vol. 50, no. 4, pp. 449–456, Apr. 2003.

[32] G. Gurun, M. Hochman, P. Hasler, and F. Degertekin, "Thermal-mechanical-noise-based CMUT characterization and sensing," *IEEE Transactions on Ultrasonics, Ferroelectrics, and Frequency Control*, vol. 59, no. 6, pp. 1267–1275, Jun. 2012.

[33] T. Gabrielson, "Mechanical-thermal noise in micromachined acoustic and vibration sensors," *IEEE Transactions on Electron Devices*, vol. 40, no. 5, pp. 903–909, May 1993.

[34] P. Behnamfar and S. Mirabbasi, "Design of a high-voltage analog front-end circuit for integration with CMUT arrays," in *2010 IEEE Biomedical Circuits and Systems Conference (BioCAS)*, Nov. 2010, pp. 298 –301.

Marco Sautto (S'14) was born in Modena, Italy, in 1988. He received the B.Sc. and M.Sc. (both with honors) in Electronic Engineering from University of Modena e Reggio Emilia (Italy) in 2010 and 2013, respectively.

Since September 2012 he is working with STMicroelectronics on the design of analog front-end ICs for MEMS ultrasound transducers.

In November 2013 he started working towards the Ph.D. in Microelectronics at University of Pavia.

Alessandro Stuart Savoia (M'03) was born in Edinburgh, Scotland (UK), in 1978. He received the Laurea and the PhD in Electronic Engineering from Università degli Studi Roma Tre, Rome, in 2003 and 2007, respectively. He has held a postdoctoral research position at the Department of Electronics Engineering of the same University since 2007. In the years 2008-2010, he participated, as a co-founder and R&D Manager, in an academic spin-off company of Roma Tre University in collaboration with the medical device company Esaote S.p.A., granted by the Italian Ministry of Education (MIUR), for the industrial exploitation of the scientific results on MEMS-based ultrasonic transducers (CMUTs), most of them achieved during his PhD and Post-Doctoral research. In 2014, he became Assistant Professor in Electronics at the Department of Engineering of Roma Tre University.

He has conducted research activity in the Acoustoelectronics Laboratory (ACULAB) mainly in the field of ultrasonic transducers and their applications. During his scientific career, he has focused on analytical and FEM modeling, design, microfabrication and packaging, characterization, electronics and system integration of MEMS-based Capacitive Micromachined Ultrasonic Transducers (CMUTs). His research interests also include piezoelectric ultrasonic transducers, and ultrasound beamforming and imaging techniques for medical and biometric applications.

Dr. Savoia has authored and co-authored about 50 papers in international journals and conferences, and two book chapters. He holds 4 international patents. He has carried out consultancy activities as a scientific advisor in the field of acoustoelectronics for several semiconductor and medical device companies.

Fabio Quaglia is acting as Team Leader for ultrasound research in a long-term joint collaboration between STMicroelectronics and University of Pavia. He was in charge as a Program Manager until 2010, following internal and external customers into products' industrialization phase, in the electro medical ultrasound market. He has been working for five years on digital parts of projects and on system simulations.

Born in 1973 in Vigevano (PV), he graduated in electronic engineering from the Università degli Studi di Pavia with a thesis work about power application in voice coil motors (VCMs) of sigma-delta modulators developed at STMicroelectronics. He has been working for STMicroelectronics since January 2001. He has written 5 papers and he is co-author of 3 patents.

Giosuè Caliano (M'00–SM'13) received an M.S. degree in electronic engineering from the University of Salerno in 1993. After receiving the degree, he served as a postgraduate fellow in the Department of Electronics of the University of Salerno, both in didactic and research fields. His interests were in developing piezoelectric pressure sensors and in measurement techniques for ceramics' characteristics. In 1995 he joined Pirelli-FOS as an Industrial Automation Engineer. In this position, he worked as design engineer for optical fiber production. Since 1997, he has worked at the ACULAB, Department of Engineering, University Roma Tre, as head of the laboratory, and since 2012, he has been Adjunct Professor of sensors and transducers. He is involved in design and characterization of micromachining ultrasonic transducers (CMUTs). In this position, he developed many types of CMUT transducers, from mono-element transducers to a 192-element probe for echographic imaging system. He obtained the first echographic images using a CMUT probe in conjunction with a commercial echographic system (2003), and he patented the new technology for cMUT fabrication called Reverse Process Technology. He is author of more than 90 papers on these fields published in international magazines and conference proceedings, plus 10 international patents. He was the founder of the International Workshop on cMUTs and has organized the event in 2001 (Roma) and 2011 (Salerno). In 2009, he was the Local Chair of the 2009 IEEE International Ultrasonics Symposium, held in Rome.

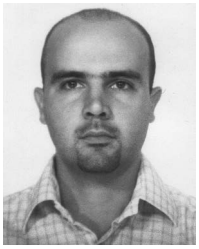

Andrea Mazzanti (S'02–M'09–SM'13) received the Laurea and Ph.D. degrees in electrical engineering from the Università di Modena and Reggio Emilia, Modena, Italy, in 2001 and 2005, respectively.

During the summer of 2003, he was with Agere Systems, Allentown, PA, USA, as an Intern. From 2006 to 2009, he was an Assistant Professor with the Università di Modena and Reggio Emilia. In January 2010, he joined the Università di Pavia where he is now an Associate Professor. He has authored over 80 technical papers. His main research interests cover device modeling and IC design for high-speed communications, RF and millimeter-wave systems.

Dr. Mazzanti was a member of the Technical Program Committee of the IEEE Custom Integrated Circuits Conference (CICC) from 2008 to 2014, IEEE European Solid-State Circuits Conference (ESSCIRC) and IEEE International Solid-State Circuits Conference (ISSCC) since 2014. He was Guest Editor for the special issue of the IEEE JOURNAL OF SOLID-STATE CIRCUITS dedicated to CICC-2013, and he is currently an Associate Editor for the IEEE TRANSACTIONS ON CIRCUITS AND SYSTEMS I